Check for updates

Raman enhancement in bowtie-shaped aperture-particle hybrid nanostructures fabricated with DNA-assisted lithography†

Kabusure M. Kabusure, (ID) ‡[a] Petteri Piskunen, (ID) ‡[b] Jiaqi Yang,[a] Veikko Linko (ID) *[b,c,d] and Tommi K. Hakala (ID) *[a]

We report on efficient surface-enhanced Raman spectroscopy (SERS) supporting substrates, which are based on deoxyribonucleic acid (DNA)-assisted lithography (DALI) and a layered configuration of materials. In detail, we used nanoscopic DNA origami bowtie templates to form hybrid nanostructures consisting of aligned silver bowtie-shaped particles and apertures of similar shape in a silver film. We hypothesized that this particular geometry could facilitate a four-fold advantage in Raman enhancement compared to common particle-based SERS substrates, and further, we verified these hypotheses experimentally and by finite difference time domain simulations. In summary, our DALI-fabricated hybrid structures suppress the background emission, allow emission predominantly from the areas of high field enhancement, and support additional resonances associated with the nanoscopic apertures. Finally, these nanoapertures also enhance the fields associated with the resonances of the underlying bowtie particles. The versatility and parallel nature of our DNA origami-based nanofabrication scheme and all of the above-mentioned features of the hybrid structures therefore make our optically resonant substrates attractive for various SERS-based applications.

1 Introduction

Various metallic nanostructures have been intensively studied owing to their ability to locally increase the incoming electromagnetic field intensity *via* plasmon resonances.[1,2] Single

[a]*Center for Photonics Sciences, University of Eastern Finland, Yliopistokatu 2, P.O. Box 111, FI-80101 Joensuu, Finland. E-mail: tommi.hakala@uef.fi*
[b]*Biohybrid Materials, Department of Bioproducts and Biosystems, Aalto University, P.O. Box 16100, FI-00076 Aalto, Finland*
[c]*LIBER Center of Excellence, Aalto University, P.O. Box 16100, FI-00076 Aalto, Finland*
[d]*Institute of Technology, University of Tartu, Nooruse 1, 50411 Tartu, Estonia. E-mail: veikko.pentti.linko@ut.ee*
†Electronic supplementary information (ESI) available: Detailed lists of materials and equipment, process parameters, additional FDTD simulations. See DOI: https://doi.org/10.1039/d3nr00616f
‡These authors contributed equally to this work.

metal nanoparticles,[3] metal particle arrangements with nanoscale gaps between the objects,[3–5] as well as apertures in metal films,[6–8] have all been shown to exhibit optically intriguing properties exploitable in applications such as sensing.[9] From these examples, particularly structures with nanoscale gaps, such as bowtie antennas[5,10,11] exhibiting intense plasmonic hotspots,[12] are attractive for surface-enhanced Raman spectroscopy (SERS)[13,14] as the Raman enhancement factor scales with the fourth power of the electric field enhancement.

However, for the Raman enhancement, also plasmonic apertures, *i.e.* metallic films perforated with nanoscopic holes,[6–8,15–21] may become highly attractive options. The reasoning is that the metal layer could potentially filter and suppress the background signal of the Raman measurement, consequently allowing the light to emanate only from the regions of high field enhancement. This could be very beneficial, as the Raman signal of interest may easily get obscured by the high background emission intensity.[22,23]

Conventionally, metallic nanostructures have been fabricated employing top-down approaches. Recently, however, affordable and highly parallel bottom-up based methods have become increasingly sophisticated. As a prime example, utilizing self-assembled deoxyribonucleic acid (DNA)-based templates has allowed fabrication of optically active materials by precision-positioning of nano-particles[24–34] or by transferring the spatial information of the DNA template to entirely inorganic structures.[35–39] Following these concepts, we have previously developed techniques that could take advantage of both the bottom-up-based DNA nanotechnology and the top-down approaches in fabrication of such optically resonant substrates. For instance, we have combined DNA origami nanostructures[40–42] as patterning templates with common micro-/nanofabrication schemes (such as thin film deposition and etching) to develop two techniques: DNA-assisted lithography (DALI)[43] and the more versatile biotemplated lithography of inorganic nanostructures (BLIN).[44] With these, we have previously patterned transparent substrates with *e.g.* bowtie-shaped metal nanoparticles with well-defined nanogaps

(<10 nm) and demonstrated their feasibility in Raman enhancement.[43,45] Owing to their highly parallel and affordable fabrication processes, DALI and BLIN may, in general, serve as intriguing alternatives to the more conventional nanopatterning approaches. However, these methods do not support aperture fabrication which could be beneficial in developing even more efficient SERS substrates as discussed above.

In this article, we show that we can modify the previous DNA-assisted lithography scheme in a way that results in a hybrid structure consisting of both aligned silver bowtie particles and nanoscale apertures of similar shape in a silver film (see DALI-fabricated hybrid structure, DHS, in Fig. 1a). We envision that this kind of a hybrid structure may exhibit very strong Raman enhancement that emerges from the intense plasmonic hotspots of the bowtie particles and the apertures as well as from spatial filtering properties of the aperture layer, allowing only the regions of high field enhancement to contribute to Raman signal.

In detail, we present four hypotheses and further show that our hybrid structure can significantly enhance Raman signals *via* four separate mechanisms (four-fold advantage): Hypothesis 1 (H1): The background emission can be suppressed by the aperture-containing metal film. Hypothesis 2 (H2): The apertures allow light emission mainly from the areas of high field enhancement, a highly desirable feature for any practical implementation of Raman substrates. Hypothesis 3 (H3): The apertures also support additional plasmonic effects that can result in significant field enhancements as such. Hypothesis 4 (H4): The presence of nanoapertures can further enhance the fields associated with the resonances of the underlying bowtie particles.

To test and verify these hypotheses experimentally, we prepared several control samples for DHS and compared their performance in the detection of rhodamine 6G (R6G), a dye commonly employed in SERS experiments. We used BLIN processing to fabricate similar sandwich-like hybrid structures on glass but with a sacrificial layer included (BLIN-fabricated hybrid structures, BHS, see Fig. 1b). This also allows completion of a lift-off step to yield bare bowtie particles on the substrate (BLIN-fabricated bowtie structures, BBS, see Fig. 1c). In addition to these, we created unpatterned samples with the same layer composition as in DHS, both with and without the metal film, to study the role of the thin films in the reduction of background emission (Fig. 1d). Furthermore, to separate the contributions of the individual and combined effects emerged from the bowtie particles and the apertures, we performed detailed finite difference time domain (FDTD simulations) for the DHS samples.
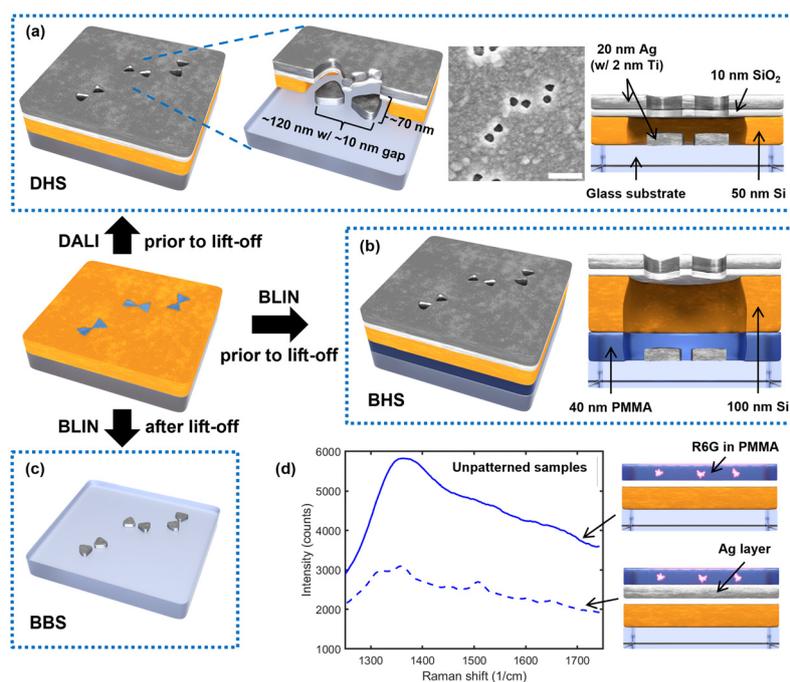

Fig. 1 An overview of the optically resonant substrates used in this study. All fabrication processes start with a silicon-coated glass (or glass-PMMA) substrate on which the DNA origami bowties have been deposited (middle left). The arrows indicate the fabrication processes used to achieve the end products a, b, and c. (a) Left: A DALI-fabricated hybrid structure (DHS) with a zoomed-in part showing the aperture-particle pair dimensions and positioning. Middle: Scanning electron microscope (SEM) image of the sample; the scale bar is 200 nm. Right: Cross-sectional model and dimensions of the bowtie aperture and particle features. (b) Left: A BLIN-fabricated hybrid structure (BHS). Right: Cross-sectional model and dimensions of the bowtie aperture and particle features. (c) BLIN-fabricated bowtie structures (BBS). (d) Comparison of the background intensities of the Raman signal for the unpatterned samples with and without a silver layer when coated with poly(methyl methacrylate) (PMMA) laced with rhodamine 6G (R6G) dye. These samples contain the same material layers and thicknesses as the DHS sample (subfigure a).

2 Methods

2.1 Fabrication of bowtie-shaped apertures and particles

The aperture-particle hybrid structures (DHS and BHS) and bowtie structures (BBS) were created using either BLIN[44] or DALI techniques,[43,46] and by employing DNA origami bowties as templates (designs, structural validation, and folding protocols for the DNA origami bowties have been reported elsewhere[43]). In brief, the DHS structures were fabricated by adapting DALI on an ordinary glass substrate and omitting the final lift-off process (Fig. 1a). To compare these DHS patterns to previously fabricated similar features,[45] BHS samples were fabricated with BLIN by also omitting the final lift-off step (Fig. 1b). Conversely, the BBS structures were created by performing the complete BLIN process on glass as shown earlier (Fig. 1c).[45] The full design, folding instructions and structural validation for the used DNA origami bowties are available in previous works.[43,44] All materials and their sources are listed in the ESI Table S1† and employed tools in Table S2.† The process parameters for all fabrication steps are given in Table S3.†

To begin processing of all samples, 0.5 mm thick borosilicate glass slides were first diced into ~10 × 10 mm^2 chips. The chips were then cleaned by soaking in hot acetone (52 °C) for 1.5 h followed by an acetone rinse and 1 min sonication in room temperature acetone. After sonication, the chips were rinsed once more with acetone, then submerged in and rinsed with isopropanol (IPA) and, finally, immediately dried with a N$_2$ flow. Next, in the case of DHS, a 50 nm a-Si layer was deposited on the cleaned glass using plasma-enhanced chemical vapor deposition (PECVD). Meanwhile, to prepare the BHS and BBS samples, instead of immediate a-Si PECVD, the chips were first spin-coated with 40 nm of sacrificial poly(methyl methacrylate) (PMMA), the PMMA was vacuum-cured, and finally, 100 nm of a-Si was deposited on the PMMA film. O$_2$ plasma treatment was then performed with a reactive ion etching (RIE) tool on all sample types to generate negative surface charges on the deposited a-Si and thus enable attachment of DNA origami templates in the next fabrication step.

Then, a solution of DNA origami in Mg^{2+} supplemented folding buffer (FOB) was prepared (5 nM bowtie DNA origami in 1× TAE buffer (40 mM Tris, 19 mM acetic acid, 1 mM ethylene diaminetetraacetic acid (EDTA)) with 100 mM Mg^{2+} at pH ~ 8.3) as shown earlier,[44] and 10 μl of the solution was drop cast on the plasma-treated a-Si surfaces. The origami solution was left to incubate, covered, in ambient conditions for 5 min and then the surfaces were washed three times with 100 μl of ddH$_2$O. After washing, the chips were dried under a N$_2$ flow. The 5 nM DNA origami concentration was chosen to avoid overcrowding and collapse of the template[44] and to enable easier comparison to previously fabricated bowtie particles.[45] The surface-attached templates were then used in the selective growth[43,47–49] of a SiO$_2$ mask layer as detailed previously.[44] A ~20 h growth time was chosen to overgrow the thin waist feature in the bowties and to thus form gapped bowtie shapes. Next, RIE was used to pierce the SiO$_2$ and a-Si layers (as well as the PMMA film in the BHS and BBS samples) to expose the underlying glass substrate, followed by physical vapor deposition (PVD) of Ti (2 nm) and Ag (20 nm) in ultra-high vacuum. Unlike in the previous DALI[43] and BLIN[44] techniques, no lift-off was performed after metal deposition for the DHS and BHS chips, which resulted in a Ag film with gapped bowtie-shaped apertures and correspondingly shaped self-aligned particles on the initial substrate (see Fig. 1a and b). The fabricated features were imaged with scanning electron microscopy (SEM) (Fig. 1a).

2.2 Unpatterned control samples

Two unpatterned control samples shown in Fig. 1d were prepared to investigate the optical responses of the used film configuration and the filtering effect (background suppression) of the employed Ag film (Fig. 1d). The samples were fabricated by following the same protocol as in the DHS sample fabrication, but the DNA origami template attachment and etching steps were omitted from the process to yield an unpatterned, but otherwise identical, stack of materials. One of the control samples was coated with Ti and Ag, while the other one was left without the metal films. After fabrication, the chips were spin-coated with a vacuum cured, ~40 nm thick PMMA layer to inhibit further oxidation of the Ag film prior to measurements.

2.3 Sample preparation for Raman experiments

The protecting PMMA layer (in case of BBS and control samples) was first removed by immersing the samples into acetone followed by a sonication step for ~10 min. Samples were then cleaned by isopropanol (IPA) for ~5 min to remove the remained PMMA residues and blow dried with a N$_2$ flow. Then, 1 ml of rhodamine 6G (R6G) solution (5 mg of R6G powder dissolved in 1 ml of ethanol) was mixed with 3.5 ml of PMMA A3 (3% 950 K PMMA in anisole (w/v) prepared by diluting 1 ml of PMMA A11 with 2.5 ml of anisole), and finally, the structures were spin-coated with this R6G solution using a spin coater at 3000 rpm for 30 s to produce a PMMA layer thickness of ~120 nm.[45] The R6G was deposited in PMMA instead of simply drop-casting and drying to both protect the analyte from environmental decay and to ensure an even analyte distribution across the samples, including any vertical structural features like the resonant hybrid cavities.

2.4 Raman measurement

A commercial Renishaw Invia Reflex Raman microscope accompanied with WiRE™ software was used to measure the Raman signals of R6G spin-coated on the structures. The sample was imaged using white light and a 50× objective lens. After selecting the area of interest to measure, the laser source was switched on to allow illumination of 785 nm laser excitation wavelength on the sample. The centre wavelength of 1500 cm^{-1}, diffraction grating of 1200 lines per mm, and 10 s of exposure time were set, while constantly controlling the laser power to achieve optimal conditions for taking the measurements. All Raman spectra were averaged from 9 measurements covering an area of 50 × 50 μm^2 (3 × 3 measurement grid with a 25 μm step size). The obtained

Raman spectra were normalized by first subtracting the smallest possible signal value from all data points in each spectrum and then dividing the resulting spectra with the highest available value in them.

2.5 Finite difference time domain (FDTD) simulations

To investigate the electric field intensity enhancements (FEs) of the proposed DHS structure, we performed full-wave simulations using the finite-difference time domain (FDTD) technique in Lumerical simulation software (Ansys). We used stabilized perfectly matched layer (PML) as simulation boundaries to minimize reflections, which guaranteed better stability for the simulation and therefore more accurate results. The electric field of the incident light was set to 1 V m^{-1}. The simulation waveband was chosen to be 100–1500 nm to cover potential Raman excitation wavelengths. The field intensity profiles were resolved for both transversely and longitudinally polarized light (x- and y-polarization, respectively; normal to the incident light). The intensity distributions are shown separately in Fig. 2 and 3, based on their different monitor locations (see also ESI Fig. S1†).

3 Results

As described in the introduction, we hypothesized in total four different mechanisms for Raman enhancement in our DHS-based system. To verify the first one, H1, we compared the Raman signals from the unpatterned samples with and without the silver layer and showed that the layer indeed blocks the background emission from the substrate effectively (Fig. 1d). It is noteworthy that even though the silver layer expectedly enhances the Raman signal of the R6G and the characteristic peaks start to appear, the overall signal is significantly reduced due to the filtering effect by the silver layer.

Further, to test the next hypotheses, we separated the individual effects of the apertures and bowtie particles by performing FDTD simulations on three cases including the bowtie-shaped apertures, the bowtie particles, and the full hybrid structure (DHS) consisting of both. Fig. 2a shows the y- and x-polarization resolved simulation results for the apertures in the absence of bowtie particles. The simulations clearly show field (intensity) hotspots on the order of 50 and 100 V^2 m^{-2}, for y- and x-polarized incident fields (1 V m^{-1}), respectively. As expected, the hotspots reside inside the aperture, which allows the signal to propagate to the collection optics (residing in the positive z-direction). One curiosity is the polarization dependence of the FE. Apparently the y-polarized incident light produces four high field intensity spots away from the bowtie center. Thus, these simulations confirm our first three hypotheses H1–H3. Intriguingly, the complete hybrid structure in Fig. 2b produces approximately similar field enhancements at the aperture region, with the exception that the maximum x-polarized enhancement at the gap of the bowtie-shaped aperture is slightly higher (120 instead of 100 V^2 m^{-2}), thus indicating that H4 might be valid as well.

In Fig. 3 we compare the FEs associated with the bowtie particles and the hybrid structure. Our structure is designed such that the broad bowtie particle resonances overlap with the excitation light (785 nm) and the Raman transitions of R6G. In Fig. 3a the sample containing only bowtie particles produces FEs on the order of 150–200 V^2 m^{-2} for both polarizations. Strikingly, the hybrid structure in Fig. 3b exhibits enormous FEs of the order of 500–600 V^2 m^{-2} at the gap region of the bowtie particles. This shows that the presence of the aperture layer in fact increases the FEs associated with the bowtie particles, fully confirming H4. Further, we carried out simulations at an x–y plane residing between the bowtie particles and apertures as a control. These plots indicate that there exists a significant interlayer coupling between plasmon resonances of the bowtie particles and the apertures, see ESI Fig. S1.† Notably, the sum of $\sqrt{\text{FE}}$ (which is equal to the electric field enhancement) for the bowtie-only and the aperture-only structures results in a smaller value than the $\sqrt{\text{FE}}$ of the hybrid structure. This suggests that the interlayer coupling could provide an additional enhancement for Raman signal measurements.

To experimentally evaluate the role of the aperture layer, we fabricated three sets of samples according to Fig. 1. Our previously introduced BLIN method[44] was used to make particle-aperture hybrid structures (BHS, Fig. 1b) and plain bowtie particles (BBS, Fig. 1c). Importantly, these two control sample sets allow a direct comparison between structures consisting of the bowtie particles only and the hybrid structures. The third set of samples was also comprised of hybrid structures, but they were fabricated via a modified and optimized DALI process (DHS, Fig. 1a). The advantage of DALI over the BLIN processing is the absence of thick PMMA and Si layers, which may then enable a stronger interlayer coupling between the aperture and the particles as shown in the simulations in Fig. 2 and 3 and ESI Fig. S1.†

In Fig. 4 we present the normalized Raman spectra for all three samples (BBS, BHS and DHS) overlaid with a layer of R6G-doped PMMA. From these three spectra we can distinguish very clear peaks at 1290, 1345, and 1490 cm^{-1} (corresponding to the wavelengths of 873, 877, and 890 nm at the 785 nm excitation), which are associated with the prominent R6G Raman transitions.[50] Due to practical reasons, we base our analysis here on normalized spectra, as the most relevant quantity, namely the signal-to-background ratio becomes most evident using this method. First, the BBS sample exhibits only very moderate Raman enhancements (light blue). Despite the significant background intensity, one can nevertheless distinguish the three relevant Raman peaks related to R6G. The presence of the silver layer, however, significantly improves signal-to-background ratio as can be seen in the BHS sample (blue). We associate this with the significant background suppression (H1) and additional hotspots related to the plasmonic enhancement in the aperture layer (H2,H3).

Finally, the optimized DHS sample starts to reveal less pronounced background-obscured spectral features of R6G around 1600 cm^{-1} (dark blue) as it takes the full advantage of
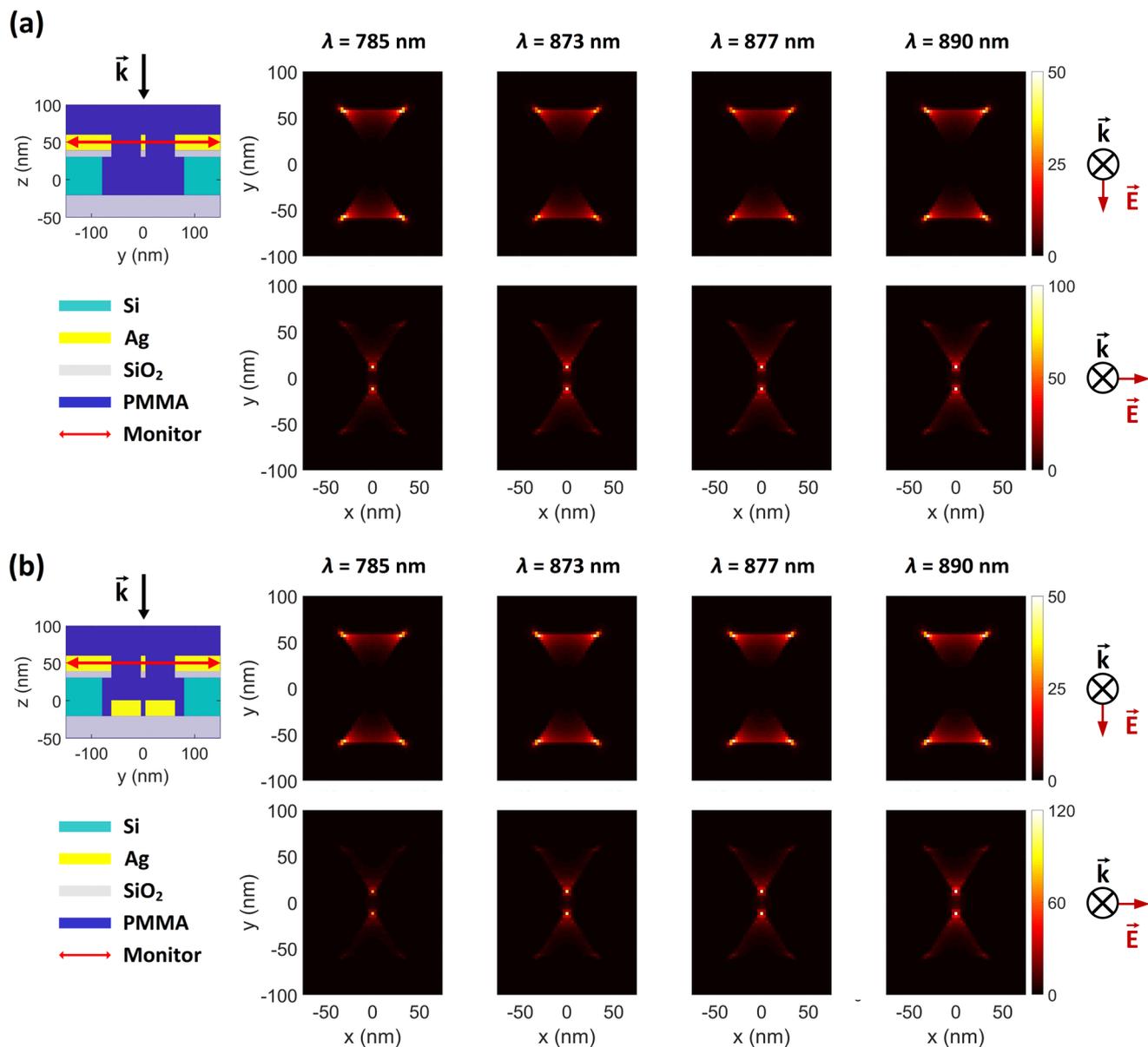
Fig. 2 FDTD simulations showing the electric field intensity profiles (in $V^2 m^{-2}$) at the apertures. The monitored area is indicated in the inset. (a) Aperture only (*i.e.* DHS without a bowtie particle) as a control. (b) DHS sample. The intensities are shown at the Raman excitation wavelength (785 nm) as well as at the Raman transition wavelengths of Rhodamine 6G (873 nm, 877 nm, and 890 nm) for both longitudinal (top panel) and transverse (bottom panel) polarizations.

all the four contributions of the new design, namely the suppressed background due to silver layer (H1), selective aperture transmission from the plasmonic hotspots (H2), plasmonic resonances related to nanoscopic apertures (H3), and additional FE stemming from the enhanced coupling of the plasmonic resonances in the aperture and particle layer (H4). This comparison of the spectra indeed manifests the outstanding performance of DHS compared to the control samples, especially to the commonly employed nanoparticle-based Raman substrates. Further, the optimized DALI structure clearly benefits from the increased interlayer coupling as compared to the BLIN reference sample.

4   Conclusions

In summary, we have shown that the presented hybrid structuring of optically resonant substrates may have several benefits compared to conventional nanoparticle-based SERS surfaces. By using DALI-fabricated bowtie particles and bowtie-shaped apertures, we were able to achieve a four-fold advantage over particle-based substrates (in our case, BLIN-fabricated bowtie particles). In addition, we observed that the DALI-fabricated hybrid structures performed better than the BLIN-fabricated hybrid ones, indicating that the interlayer coupling strength between the particles and the apertures depends on
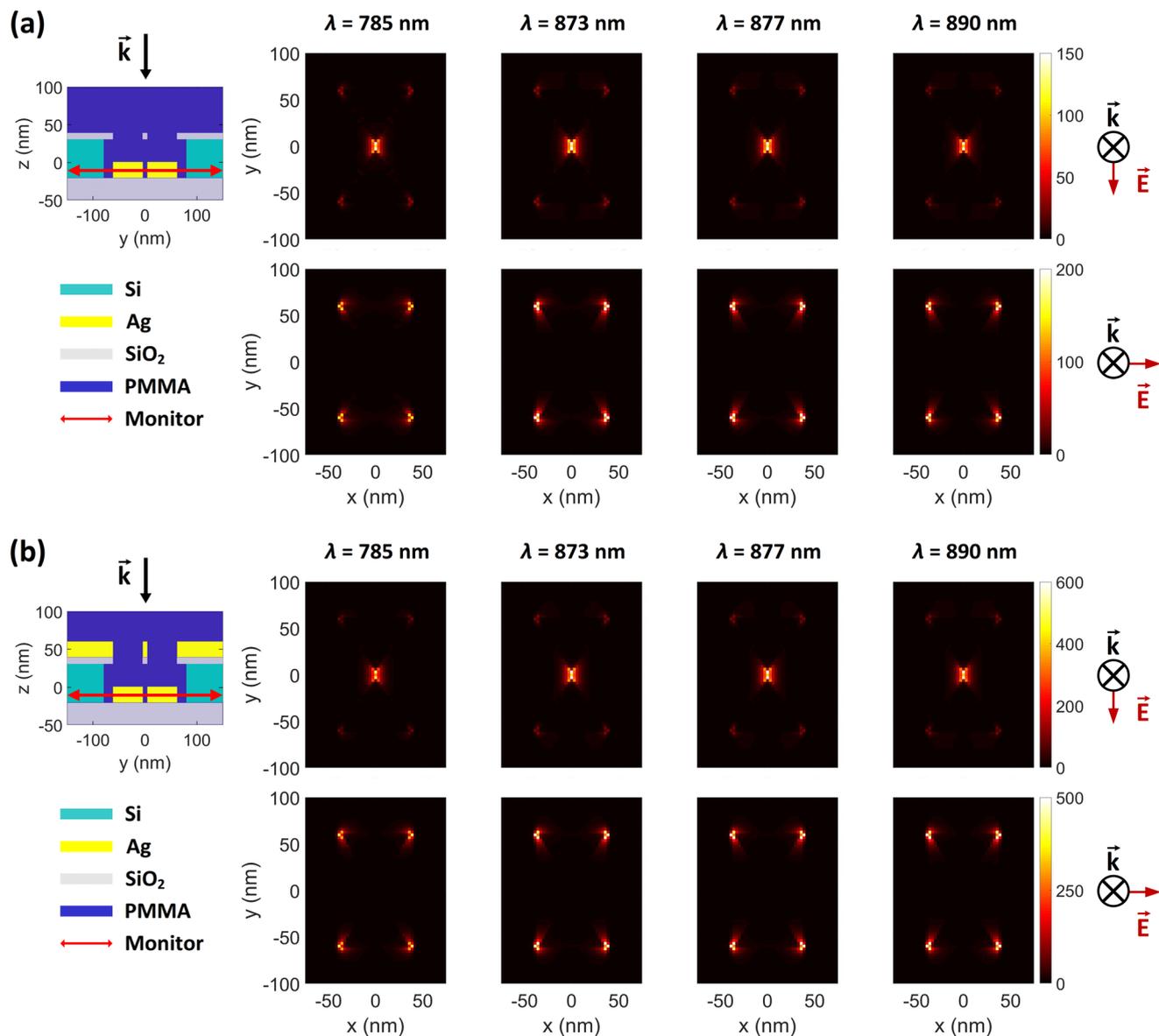
Fig. 3 FDTD simulations showing electric field intensity profiles (in V^2 m^{-2}) at the bowtie particles. The monitored area is indicated in the inset. (a) Bowtie only (*i.e.* DHS without the aperture) as a control. (b) DHS sample. The intensities are shown at the Raman excitation wavelength (785 nm) as well as at the Raman transition wavelengths of Rhodamine 6G (873 nm, 877 nm, and 890 nm) for both longitudinal (top panel) and transverse (bottom panel) polarizations.

the distance between the layers. This provides yet another degree of freedom in our system as it could allow tuning of the interlayer coupling by design (in practice this is limited by the thickness of the PVD-deposited metal layer and silicon etching selectivity in RIE).

Commonly established methodology in SERS is based on drop-casting and drying of analyte on the substrate, instead, in our case the analyte molecules are homogeneously distributed in the spin-coated PMMA layer. Thus, the results obtained using these two different methods are not directly comparable. However, it is expected that our presented approach should produce high SERS enhancement also in the case of drop-

casting and drying of the analyte molecules. This is due to the fact that the field enhancements are significant in the immediate vicinity of the apertures and the highest at the surface of the particles, *i.e.*, at the locations where the molecules are supposed to get attached. Moreover, the dielectric environment can be made similar to the presented case by filling the cavities with *e.g.* index-matching liquids. Pushing the methodology to its limits and quantifying the threshold of trace amount detection remain interesting scopes for further studies.

Currently, our method is based on single, discrete DNA origami structures, however, it is noteworthy that modular
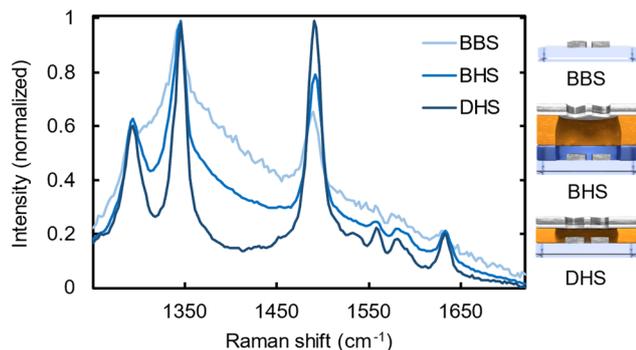
Fig. 4 Comparison of normalized R6G Raman spectra measured on DHS, BHS and BBS substrates.

DNA origami units can also assemble into hierarchical arrays and macroscopic lattices.[51] Therefore, the presented parallel and affordable[52,53] DNA origami-based fabrication schemes could potentially be extended to highly ordered hybrid structures with even more intriguing optical features.

Conflicts of interest

There are no conflicts to declare.

Acknowledgements

References

1 C. Tabor, R. Murali, M. Mahmoud and M. A. El-Sayed, *J. Phys. Chem. A*, 2009, **113**, 1946–1953.
2 L. Novotny and N. Van Hulst, *Nat. Photonics*, 2011, **5**, 83–90.
3 E. Hao and G. C. Schatz, *J. Chem. Phys.*, 2004, **120**, 357–366.
4 W. Rechberger, A. Hohenau, A. Leitner, J. Krenn, B. Lamprecht and F. Aussenegg, *Opt. Commun.*, 2003, **220**, 137–141.
5 A. Sundaramurthy, K. B. Crozier, G. S. Kino, D. P. Fromm, P. J. Schuck and W. E. Moerner, *Phys. Rev. B: Condens. Matter Mater. Phys.*, 2005, **72**, 165409.
6 T. W. Ebbesen, H. J. Lezec, H. F. Ghaemi, T. Thio and P. A. Wolff, *Nature*, 1998, **391**, 667–669.
7 L. Martín-Moreno, F. J. García-Vidal, H. J. Lezec, K. M. Pellerin, T. Thio, J. B. Pendry and T. W. Ebbesen, *Phys. Rev. Lett.*, 2001, **86**, 1114–1117.
8 N. Djaker, R. Hostein, E. Devaux, T. W. Ebbesen, H. Rigneault and J. Wenger, *J. Phys. Chem. C*, 2010, **114**, 16250–16256.
9 J. Mejía-Salazar and O. N. Oliveira Jr., *Chem. Rev.*, 2018, **118**, 10617–10625.
10 D. P. Fromm, A. Sundaramurthy, P. J. Schuck, G. Kino and W. E. Moerner, *Nano Lett.*, 2004, **4**, 957–961.
11 A. Kinkhabwala, Z. Yu, S. Fan, Y. Avlasevich, K. Müllen and W. E. Moerner, *Nat. Photonics*, 2009, **3**, 654–657.
12 S. Dodson, M. Haggui, R. Bachelot, J. Plain, S. Li and Q. Xiong, *J. Phys. Chem. Lett.*, 2013, **4**, 496–501.
13 K. Kneipp, H. Kneipp, I. Itzkan, R. R. Dasari and M. S. Feld, *J. Phys.: Condens. Matter*, 2002, **14**, R597.
14 K. Hering, D. Cialla, K. Ackermann, T. Dörfer, R. Möller, H. Schneidewind, R. Mattheis, W. Fritzsche, P. Rösch and J. Popp, *Anal. Bioanal. Chem.*, 2008, **390**, 113–124.
15 T. J. Kim, T. Thio, T. W. Ebbesen, D. E. Grupp and H. J. Lezec, *Opt. Lett.*, 1999, **24**, 256–258.
16 J. Dintinger, S. Klein and T. W. Ebbesen, *Adv. Mater.*, 2006, **18**, 1267–1270.
17 H. Wei, U. Håkanson, Z. Yang, F. Höök and H. Xu, *Small*, 2008, **4**, 1296–1300.
18 H. Guo, T. P. Meyrath, T. Zentgraf, N. Liu, L. Fu, H. Schweizer and H. Giessen, *Opt. Express*, 2008, **16**, 7756–7766.
19 M. Schnell, A. Garcia-Etxarri, J. Alkorta, J. Aizpurua and R. Hillenbrand, *Nano Lett.*, 2010, **10**, 3524–3528.
20 R. A. Jensen, I.-C. Huang, O. Chen, J. T. Choy, T. S. Bischof, M. Lončar and M. G. Bawendi, *ACS Photonics*, 2016, **3**, 423–427.
21 Y. Chen, Y. Chen, J. Chu and X. Xu, *ACS Photonics*, 2017, **4**, 567–575.
22 P. Matousek, M. Towrie and A. W. Parker, *J. Raman Spectrosc.*, 2002, **33**, 238–242.
23 D. Wei, S. Chen and Q. Liu, *Appl. Spectrosc. Rev.*, 2015, **50**, 387–406.
24 A. Kuzyk, R. Schreiber, Z. Fan, G. Pardatscher, E.-M. Roller, A. Högele, F. C. Simmel, A. O. Govorov and T. Liedl, *Nature*, 2012, **483**, 311–314.
25 G. P. Acuna, F. M. Möller, P. Holzmeister, S. Beater, B. Lalkens and P. Tinnefeld, *Science*, 2012, **338**, 506–510.
26 V. V. Thacker, L. O. Herrmann, D. O. Sigle, T. Zhang, T. Liedl, J. J. Baumberg and U. F. Keyser, *Nat. Commun.*, 2014, **5**, 3448.
27 E.-M. Roller, L. V. Besteiro, C. Pupp, L. K. Khorashad, A. O. Govorov and T. Liedl, *Nat. Phys.*, 2017, **13**, 761–765.
28 M. Pilo-Pais, G. P. Acuna, P. Tinnefeld and T. Liedl, *MRS Bull.*, 2017, **42**, 936–942.

29 C. Heck, J. Prinz, A. Dathe, V. Merk, O. Stranik, W. Fritzsche, J. Kneipp and I. Bald, *ACS Photonics*, 2017, **4**, 1123–1130.

30 P. Zhan, T. Wen, Z.-g. Wang, Y. He, J. Shi, T. Wang, X. Liu, G. Lu and B. Ding, *Angew. Chem., Int. Ed.*, 2018, **57**, 2846–2850.

31 B. Shen, M. A. Kostiainen and V. Linko, *Langmuir*, 2018, **34**, 14911–14920.

32 A. Kuzyk, R. Jungmann, G. P. Acuna and N. Liu, *ACS Photonics*, 2018, **5**, 1151–1163.

33 A. T. M. Yeşilyurt and J.-S. Huang, *Adv. Opt. Mater.*, 2021, **9**, 2100848.

34 K. Tapio, A. Mostafa, Y. Kanehira, A. Suma, A. Dutta and I. Bald, *ACS Nano*, 2021, **15**, 7065–7077.

35 E. P. Gates, A. M. Dearden and A. T. Woolley, *Crit. Rev. Anal. Chem.*, 2014, **44**, 354–370.

36 M. Bathe, L. A. Chrisey, D. J. C. Herr, Q. Lin, D. Rasic, A. T. Woolley, R. M. Zadegan and V. V. Zhirnov, *Nano Futures*, 2019, **3**, 012001.

37 A. Heuer-Jungemann and V. Linko, *ACS Cent. Sci.*, 2021, **7**, 1969–1979.

38 I. V. Martynenko, V. Ruider, M. Dass, T. Liedl and P. C. Nickels, *ACS Nano*, 2021, **15**, 10769–10774.

39 L. Hui, R. Bai and H. Liu, *Adv. Funct. Mater.*, 2022, **32**, 2112331.

40 P. W. K. Rothemund, *Nature*, 2006, **440**, 297–302.

41 S. M. Douglas, H. Dietz, T. Liedl, B. Högberg, F. Graf and W. M. Shih, *Nature*, 2009, **459**, 414–418.

42 S. Dey, C. Fan, K. V. Gothelf, J. Li, C. Lin, L. Liu, N. Liu, M. A. Nijenhuis, B. Saccà, F. C. Simmel, H. Yan and P. Zhan, *Nat. Rev. Methods Primers*, 2021, **1**, 13.

43 B. Shen, V. Linko, K. Tapio, S. Pikker, T. Lemma, A. Gopinath, K. V. Gothelf, M. A. Kostiainen and J. J. Toppari, *Sci. Adv.*, 2018, **4**, eaap8978.

44 P. Piskunen, B. Shen, A. Keller, J. J. Toppari, M. A. Kostiainen and V. Linko, *ACS Appl. Nano Mater.*, 2021, **4**, 529–538.

45 K. M. Kabusure, P. Piskunen, J. Yang, M. Kataja, M. Chacha, S. Ojasalo, B. Shen, T. K. Hakala and V. Linko, *Nanoscale*, 2022, **14**, 9648–9654.

46 P. Piskunen, B. Shen, S. Julin, H. Ijäs, J. J. Toppari, M. A. Kostiainen and V. Linko, *J. Visualized Exp.*, 2019, e60313.

47 S. P. Surwade, F. Zhou, B. Wei, W. Sun, A. Powell, C. O'Donnell, P. Yin and H. Liu, *J. Am. Chem. Soc.*, 2013, **135**, 6778–6781.

48 F. Zhou, B. Michael, S. P. Surwade, K. B. Ricardo, S. Zhao and H. Liu, *Chem. Mater.*, 2015, **27**, 1692–1698.

49 B. Shen, V. Linko and J. J. Toppari, DNA-Assisted Molecular Lithography, in *DNA Nanotechnology. Methods in Molecular Biology*, Humana Press, New York, NY, 2018, vol. 1811, pp. 299–314.

50 K. Alam, K. M. Kabusure, B. O. Asamoah, T. Nuutinen, M. Baah, S. Mohamed, A. Matikainen, J. Heikkinen, H. Rekola, M. Roussey, M. Kuittinen and T. K. Hakala, *Nanoscale*, 2020, **12**, 23166–23172.

51 Y. Xin, B. Shen, M. A. Kostiainen, G. Grundmeier, M. Castro, V. Linko and A. Keller, *Chem. – Eur. J.*, 2021, **27**, 8564–8571.

52 F. Praetorius, B. Kick, K. L. Behler, M. N. Honemann, D. Weuster-Botz and H. Dietz, *Nature*, 2017, **552**, 84–87.

53 Q. Zhang, K. Xia, M. Jiang, Q. Li, W. Chen, M. Han, W. Li, R. Ke, F. Wang, Y. Zhao, Y. Liu, C. Fan and H. Gu, *Angew. Chem., Int. Ed.*, 2023, **62**, e202212011.